

Super-resolution Line Scan Image Sensor for Multimodal Microscopy

Chengzhi Winston Liu, Arshya Feizi, Navid Sarhangnejad, Glenn Gulak and Roman Genov

Abstract—A low-cost contact scanning microscope is presented which performs optical imaging of millimeter-scale samples with multiple sensory modalities at a spatial resolution better than the pixel size in both x and y dimensions. The $7.5\text{ mm} \times 3.2\text{ mm}$ $0.35\text{ }\mu\text{m}$ CMOS image sensor is comprised of 214 scanning lines of 256 pixels, each line horizontally shifted by 300 nm with respect to the adjacent lines. When scanning in the y dimension, this results in a staircase-like staggered-pixels organization with an effective spatial resolution in the x dimension of less than the pixel size, with a theoretical limit of 300 nm, subject to the light diffraction limit and to photodiode size-dependent spatial aliasing. The height of the resulting pixel "staircases" is capped at 2.5 mm by wrapping the 215th row back to the first row, yielding an approximately $2\text{ mm} \times 2.5\text{ mm}$ instantaneous scanning window size. The spatial resolution in the y dimension is set by the sample scanning rate and the frame rate, subject to the same limitations. Integration of multiple scanning lines naturally lends itself to inclusion of multiple sensory modalities, with five modalities included as an example: high-resolution (up to 300 nm), fluorescence-sensitive, and triple-orientation light polarization-sensitive pixels. The resulting modified scanning pattern is digitized by on-chip column-parallel 2nd-order Delta-Sigma ADCs with ENOB of 9.1 and is reconstructed into a full-resolution image in software. Experimental measurements, where contact-scanning is emulated by the sample image moving on an LCD monitor and projected through a lens, support the validity of the presented concept.

I. INTRODUCTION

Microscopes have been used for centuries as a vital tool for biomedical diagnosis and research. Based on their principal of operation, they can be classified into two main categories: optical and non-optical microscopes. In optical (light) microscopes, a light source with known spectrum, intensity, and polarity is used to illuminate the sample of interest. As a result, the sample then emits light which is collected using a combination of light filters, lenses, and mirrors. Based on the type of light microscope, the collected light from the sample can be the result of a light-triggered chemical phenomenon such as in fluorescent imaging microscopes, polarity change such as in polarization microscopes, light dispersion, etc. With each having their pros and cons, the resolution of light microscopes is fundamentally constrained by the numerical aperture of their utilized lenses and ultimately, the inevitable light diffraction phenomenon which limits their resolution to hundreds of nanometers [1]. This limitation is addressed in non-optical microscopes which utilize alternative means to probe their sample. For example, in scanning electron microscopes (SEMs) a focused electron beam scans the sample's surface and generates signals which contain information about its surface topography and composition with a resolution of less than 1 nm [2].

Although the aforementioned microscopes enjoy state-of-the-art resolution, not only are they expensive and bulky, but they are also fragile and require careful handling, rendering them unsuitable for portable point-of-care applications. This limitation is addressed in low-cost small form-factor lens-less imaging systems [3]. In such a contact imaging system the specimen is placed directly on top of a CMOS/CCD (charge-coupled-devices) image sensor. A light source is placed above the image sensor to illuminate the sample. In these systems most specimens of interest are translucent after staining [4]. Therefore, a shadow of the sample is projected on the image sensor. The resolution of such a system is limited by the pixel size of the image sensor, today ranging from $1\text{ }\mu\text{m}$ to $100\text{ }\mu\text{m}$ [5], [6], [7], [8], [9]. Another major limitation of existing microscopes is that, typically, they can not be easily used to image several sensory modalities simultaneously (e.g, fluorescence and polarization). To overcome these limitations, in this work, a multimodal scanning contact microscope (SCM) is introduced which achieves sub-pixel resolution and multimodal imaging in CMOS using these key techniques:

- 1) Spatial oversampling: [10], [11], [12], [13] In this technique, the idea is to take multiple low-resolution images of the specimen which are spaced by less than a pixel size with respect to each other. The images are then combined to approximate a single image with a resolution higher than each image. Although this method is simple to implement in terms of hardware, the resolution of the ultimate high-resolution image is dependent on the displacement between images, the number of images, and whether they are scattered sufficiently in both dimensions of the image.
- 2) Photodiode aperture reduction: In this method, a small photodiode is utilized to create small apertures. The system is configured such that light from the specimen is collected through a small aperture as opposed to an entire larger photodiode, increasing the resolution to the aperture size. Compared to method (1) above, this reduces or eliminates spatial aliasing. However, this comes at the cost of lower signal-to-noise ratio (SNR) since the photodiodes are mostly covered. A commercially available CMOS image sensor with additional labor-expensive post-processing steps to fabricate the aperture was previously demonstrated [14] with an additional cost of resource underutilization since only one or few pixel rows were used.
- 3) Multimodal scanning pixels: A novel multi-modality line scanning pixel organization is proposed which enables

the SCM to integrate multiple pixel types, each optimized for a particular technique of light microscopy. In this work, for proof of concept, the presented SCM includes one small-aperture ($300\text{ nm} \times 1200\text{ nm}$) pixel, one pixel for fluorescence imaging, and three pixels for polarized light imaging.

A comparison among the spatial resolution, field of view, and imaging modalities of unconventional microscopes using the aforementioned techniques can be found in Table I.

The rest of this paper is organized as follows. A background on sub-pixel resolution imaging and line scanning techniques is given in Section II. Section III describes the line-scanning technique used in this work. Section IV presents the VLSI architecture of the system. The measurement results are explained in Section V.

II. BACKGROUND

A. Sub-pixel resolution via spatial oversampling

One method of sub-pixel resolution imaging is to oversample the scene/sample spatially by taking multiple images of the same scene/sample with spatial exposure shifts smaller than one pixel size. A pixel super resolution algorithm (SRA), described in detail in [11], combines these data to approximate a high-resolution image. Several techniques have been proposed to enable sub-pixel shifted data acquisition. In [10], mechanical coils and actuators are used to slightly shift the location of an LED which is used as the light source to illuminate the sample. However, this method results in additional power wasted in the actuators and a relatively unstable setup due to moving system components. This problem is addressed in opto-fluidic microscopes (OFM) [5]. As illustrated in Fig. 1, one contact imaging method is to flow samples in close proximity of the image sensor's surface using a microfluidic channel. This inherent movement in the system is exploited in [12] to acquire multiple images with sub-pixel shifts by increasing the frame rate of the image sensor such that during the time between two consecutive images, the sample's displacement is much smaller than the pixel pitch. Nonetheless, this method results in sub-pixel shifts on only the movement axis which reduces the efficacy of the SRA. Also, the image data is obtained from a 2D image sensor where, in fact, all of required information can be extracted from a single row of pixels (a line scanner) as described next.

B. Principle of line-scanning

Similar to the operation concept of a traditional office document scanner, in an OFM a line scanner can be used to capture the ultimate image one row at a time as the sample moves over the image sensor. The acquired *row* images are later stacked vertically to generate the desired 2D image. Assuming a constant laminar flow rate within the microchannel, the maximum allowable delay between consecutive image captures is the pixel pitch divided by the flow rate.

Various techniques have been devised to improve the quality of a line scanner's image output in industrial applications. In [18], a wide-field image is obtained while eliminating the

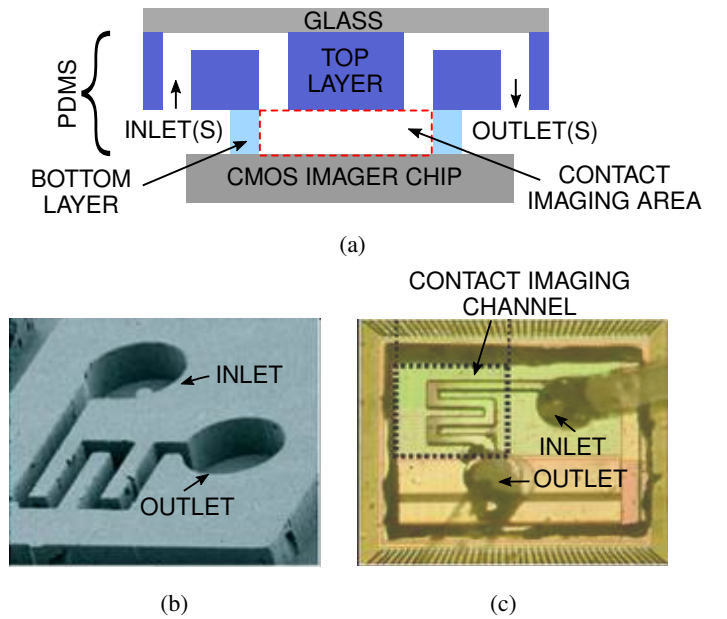


Fig. 1: Illustration of a contact imaging technique we have previously devised where micro-samples to be imaged are delivered to the surface of a CMOS image sensor via a microfluidic structure [5]. (a) Illustration of a cross-section of a CMOS-microfluidic contact imaging microsystem. (b) SEM micrograph of an example of the bottom layer of the microfluidic chamber with a snaking maze-shaped channel, fabricated from a flexible organic polymer polydimethylsiloxane (PDMS). (c) Top-view micrograph of the microfluidic channel shown in subfigure (b) sealed against a CMOS image sensor die surface.

need to either create a prohibitively large sensor or reduce its pixel size which, in turn, reduces the SNR of the image. Three parallel line scanners are placed on the movement axis with partially overlapping segments. The images from the three scanners are then combined to yield a single high-resolution, wide-field image; the overlapping portions determine the offset and rotation of the object.

In [19], two parallel lines of pixels, spaced on the movement axis, capture identical images which are later combined to generate a single output image with an enhanced light response.

In [20], two rows of a conventional 2D pixel array are given a *half*-pixel pitch lateral shift to capture two images spaced laterally by a half-pixel. The two images are combined to create a single image with a spatial resolution better than each individual line scanner.

The line scanning scheme can be further exercised by considering the following: in theory, the line of pixels need not be in a perfectly horizontal line perpendicular to the direction of movement. In other words, each pixel may be placed in an arbitrarily location along the movement axis without compromising the total collected data from the scanner (albeit the image reconstruction algorithm must be customized for the particular pixel arrangement). This idea is used in [21] to construct a color-sensing line scanner. This is accomplished by rearranging the pixels in 4-row staggered periods where, a

TABLE I: Comparison with existing unconventional microscopic imaging systems.

Specifications	Bishara <i>et. al</i> [13]	Cui <i>et. al</i> [14]	Zhu <i>et. al</i> [15]	Breslauer <i>et. al</i> [16]	Switz <i>et. al</i> [17]	Current work
Operating Principle	Digital in-line holographic microscopy	Spatial oversampling	Wide-field fluorescent imaging	Brightfield and fluorescence imaging	Wide-field imaging	Staggered pixel multi-line scanner
Imager/Form Factor	Micron CMOS technology with 2.2 μm pixels	Micron CMOS technology with 9 μm pixels	Cell phone camera with defocusing lens attachment	Cell phone camera with microscope attachment	Cell phone camera with attached reversed lens	Custom 0.35 μm CMOS Imager
Spatial Resolution	0.6 μm	0.8 μm	10 μm	1.2 μm	5 μm	0.3 μm
Field of View	24 mm^2	0.05 mm^*	81 mm^2	n/a	10 mm^2	2.48 mm^*
Modalities #	1	1	1	2	1	5**

* The scanning nature of the microscope results in an unconstrained image length.

** The system is capable of simultaneously imaging all 5 modalities.

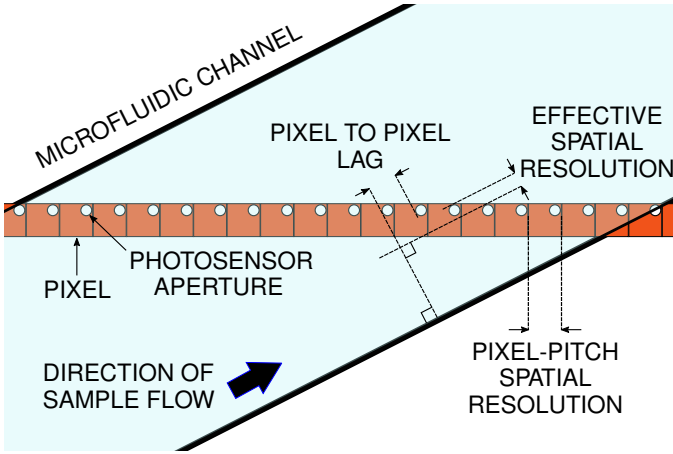


Fig. 2: Setting the angle of the sample movement axis with respect to a row of pixels in a commercially available CMOS imager [14]. This mimics a truly staggered line scanner organization presented here, but with significant limitations as described in this section.

color filter is placed on each row and the period is repeated for the entire length of the line; each row captures an image corresponding to its respective color filter. The filtered images are then combined to obtain a single color image.

Staggering has also been used for the purpose of sub-pixel resolution imaging as discussed next.

C. Sub-pixel resolution via pixel staggering

In [14] pixels of a conventional commercial 2D CMOS image sensor were first coated with opaque material. Then a single small aperture with a diameter of D_A was etched over a specific point of each pixel's photodiode. As depicted in Fig. 2, the angle between the movement axis and a row

of the pixel array was calculated such that the apertures on the column align in a stair-case formation to form what would effectively be a line scanner with aperture-sized pixels arranged in a staggered format with respect to the movement axis. The sample moves over the newly-constructed staggered line of *apertures*, obviating the resolution limitation posed by the size of the original pixels. Using this technique, the effective pixel size is shrunk to the size of the aperture, significantly improving the resolution of the line sensor. This comes at the cost of reduced SNR since the light response has decreased whilst the total pixel noise remains constant. This is a key drawback of this system [14]. Also, this approach relies on post-processing on the CMOS image sensor, adding cost and complexity to the system. Moreover, commercial CMOS image sensors are not optimized for this method since there is an inverse relationship between the required number of pixels in a column and the aperture size. Holding the field-of-view constant, the required height of the pixel column increases by the factor by which the aperture size shrinks, which raises a practical limitation on either the microscope's field-of-view or the aperture diameter (i.e. resolution). Also, all but one column of the 2D image sensor's pixels remain unused which is a waste of silicon area. Finally, only one sensory modality can be used.

In this work, a novel staggered pixel layout organization based on the described line scanning principles is presented which enables the SCM to achieve multimodal sub-pixel resolution via techniques listed in Section I simultaneously while addressing their shortcomings:

- 1) The sample is spatially oversampled in both the movement axis and its perpendicular axis. Displacements along the movement axis are controlled by displaying the target sample on a standard desktop monitor to emulate sample movement in a microfluidic channel and shifting

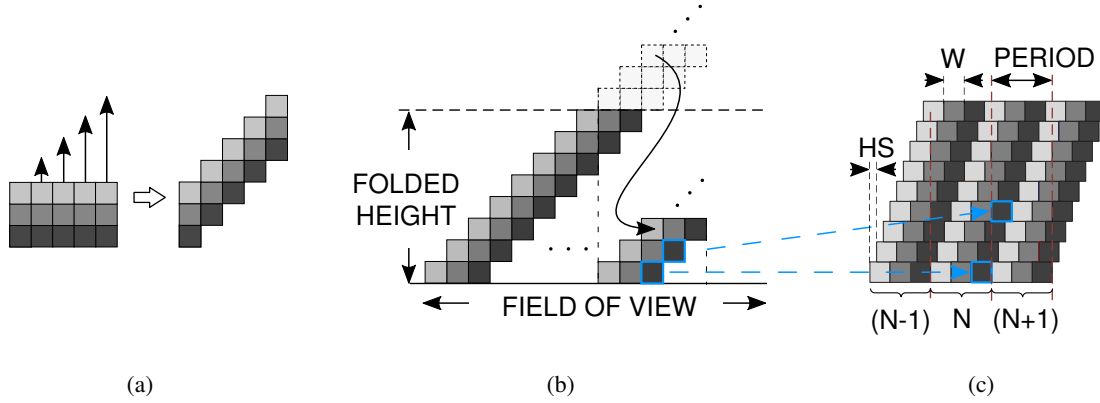


Fig. 3: a) The concept of staggering multimodal pixels. b) Folded staggering of pixels. c) Detailed drawing of the multimodal folded-staggered pixel array for three multimodal pixel spatial periods: $N-1$, N , and $N+1$. W is the width of a single pixel and HS is the horizontal shift between rows.

it by fractions of the pixel height. Note that since flow rates within microfluidic channels can be tightly controlled, this models well the efficacy of the SCM in a real contact imaging setting. Displacements perpendicular to the movement axis are strictly determined by the pixel layout.

- 2) An inherent high-resolution image is acquired using photodiodes much smaller than the pixel size which are aligned to form a staggered-pixel line scanner; this is achieved without CMOS post-processing.
- 3) Multiple imaging modalities are included in the same design, so that they are co-registered simultaneously during a single scan.

Therefore, in cases where the sensor's high sensitivity is not crucial (e.g. medium-high lighting conditions), the SCM is capable of producing an inherent sub-pixel resolution image using the photodiode aperture reduction technique; if high sensitivity (SNR) is desirable and/or critical (e.g. low lighting conditions) 2D spatial oversampling achieves sub-pixel resolution imaging. The image resolution from the pixels optimized for polarized-light imaging and fluorescence imaging are enhanced by such 2D spatial oversampling. Moreover, by integrating a number of pixel types onto the scanner, no silicon area is wasted as opposed to the case with commercial imagers [14].

III. PRINCIPLE OF MULTIMODAL STAGGERED SCANNING

Conventionally, in order to image a sample using a particular imaging modality (e.g. polarized light, fluorescence, etc.) a 2D image sensor in which its pixels are optimized for that specific configuration is used and/or optical splitters and multiple optical filters are required. In other words, if multiple images in different modalities are required from the same sample, that many sensors or bulky optical components are needed. Not only is this inefficient, but more importantly, many types of samples may be destroyed after being imaged, rendering the task of re-imaging using a different modality difficult or impossible.

A multimodal staggered line scanning system is proposed which performs simultaneous imaging of a sample in different modalities with sub-pixel resolution.

A. Multimodal line scanner

As described in detail in Section II, if a sample's one-dimensional movement is an inherent feature of an imaging system (e.g. in an OFM), the complete data set required to create a 2D image of the sample can be obtained using one row of pixels alone. Subsequently, in order to create a multimodal sensor, it is possible to integrate multiple rows of pixels, each optimized for a particular imaging modality, onto the sensor without making the silicon die prohibitively large. If, for example, three imaging modalities are desired, three rows of pixels can be placed perpendicular to the movement axis, where each row of pixels is optimized for a particular modality. As the sample flows over the sensor, data from each row is collected individually to create three separate images, each corresponding to one imaging modality. At this point, an image sensor is configured which consists of three rows with three pixel types as shown on the left of Fig. 3a.

As described in Section II-B, the physical location of the pixels of a row along the movement axis is not important as long as the mapping of each pixel to its respective column of the frame is known, the sample speed (assuming fixed) is known and the sample is completely passed over the sensor. Therefore, as shown in Fig 3a, right, the pixels of each column of the 2D multimodal line scanner can be pushed along the movement axis to form a staggered pixel arrangement for each particular type of pixel, while the theory of line scanning remains intact. For the sake of clarity, note that each row of the newly formed 2D array consists of *all* pixel types (three in this example).

In [14], the field of view in a staggered line sensor is limited to the $D_A \times N_{pixel}$ where D_A is the aperture size (or generally, the effective pixel size) and N_{pixel} is the number of pixels in a row. This limitation is eliminated in the presented work by introducing the concept of folded-staggered pixels. As shown in Fig. 3b, once the staggered line of pixels reach a predefined

maximum height, the rest of the line can be shifted down to start a new staggered *period* of pixels without disrupting the line scanning concept. This eliminates the practical limitation on the maximum number of pixels that can be placed in a staggered line (i.e. the width of the frame) without increasing the height of the pixel array to prohibitive die sizes.

B. Staggering and spatial oversampling

As explained in Section II, one method to obtain a sub-pixel resolution image is to oversample the scene by taking a set of low-resolution images which are shifted with respect to each other by less than a pixel size. Subsequently, the super resolution algorithm generates a high-resolution image using the low-resolution images. This method of sub-pixel resolution imaging can be performed in a staggered line sensor. Each row of pixels in Fig. 3b can be shifted apart vertically (by two empty rows in this example) along the movement axis to make space for additional rows. As shown in Fig. 3c, each newly added row (two in this case) is shifted horizontally with respect to the row below by a *set fraction HS* of the pixel width W ($HS = W/3$ in this example). This arrangement yields multiple images shifted horizontally with respect to each other by HS . To summarize, Fig. 3c depicts an example for three modality images, shifted by a third of a pixel width. For this, two additional rows are inserted in between each two rows of Fig. 3b, shifted horizontally by $HS = W/3$. The first image is created by compiling rows 1, 4, 7, ..., $3k + 1$, which create an image no different than that of Fig. 3b. The second image is create using rows 2, 5, 8, ..., $3k + 2$. The third image is generated using rows 3, 6, 9, ..., $3k$.

To generate images with sub-pixel shifts along the movement axis, the frame rate of the sensor is increased such that the time gap between two consecutive frames is less than the time it takes for the sample to completely pass over one pixel (equally effective is to reduce the movement speed of the sample while keeping frame-rate constant).

Using these techniques, multiple images with sub-pixel shifts on the movement axis and its perpendicular axis are obtained. These slightly shifted frames serve as raw data for the SRA in post-processing.

To generalize, Fig. 3c shows the conceptual architecture of a folded-staggered multimodal line sensor. Each two adjacent pixels of a line are separated by the number of rows in between them, N_{row} , which is determined by the horizontal shift between rows (HS). HS also determines the number of sub-pixel shifted images which are fed to the super-resolution algorithm. As highlighted in Fig. 3c, the condition for not losing data when folding a line (i.e. starting a new period) is that the first pixel of the N^{th} period be horizontally aligned with the last pixel of the $(N - 1)^{th}$ period such that it corresponds to a vertical shift of the pixel which would be the very *next* pixel to the $(N - 1)^{th}$ period. This requires each pixel type to cross the entire width of the period diagonally. Therefore, the height of the array is calculated as follows:

$$\begin{aligned} W_{Period} &= M \times W \\ N_{Height} &= \frac{W_{Period}}{HS} \end{aligned}$$

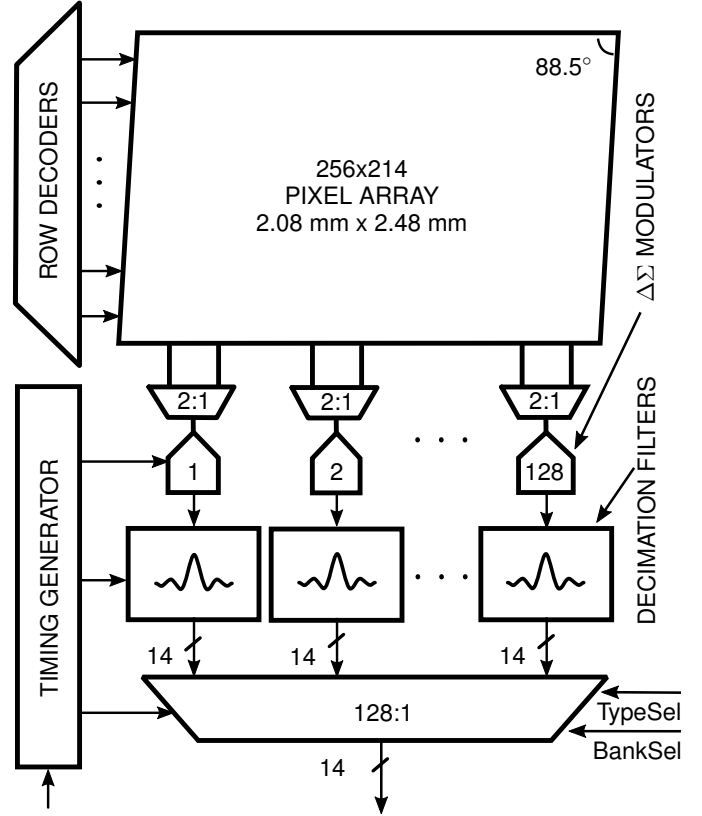


Fig. 4: CMOS scanning contact microscope VLSI architecture and floorplan.

$$H_{Array} = N_{Height} \times H \quad (1)$$

where M is the number of modalities (pixel types), W is the width of the pixel, H is the pixel height, HS is the row-to-row horizontal shift, W_{Period} is the width of a pixel period, N_{Height} is the number of pixels required to cover one period width with a diagonal stack, and H_{Array} is the required height of the pixel array. Equation (1) shows that the necessary height of the array is directly affected by the number of pixel *types*. Adding one pixel type to the period increases the number of rows by a factor of $\frac{W}{HS}$. Decreasing HS also increases the height since it will take more rows to cover the entire width of the period.

IV. VLSI ARCHITECTURE

The CMOS prototype was fabricated in a $0.35\mu\text{m}$ imaging process. The chip architecture is depicted in Fig. 4. It consists of a row decoder, a multimodal pixel array, read-out circuitry, and a readout timing generator. The complete pixel array consists of 214 rows and 256 columns. The array height is 2.5 mm. Since HS directly affects the required height of the pixel array, it was chosen based on the maximum allowable aspect ratio of the chip. Therefore, if the width of the pixel array were increased, HS could be smaller, subject to limitations in SNR and light diffracting limits. The staggered pixel array is driven by the row decoders and read out using

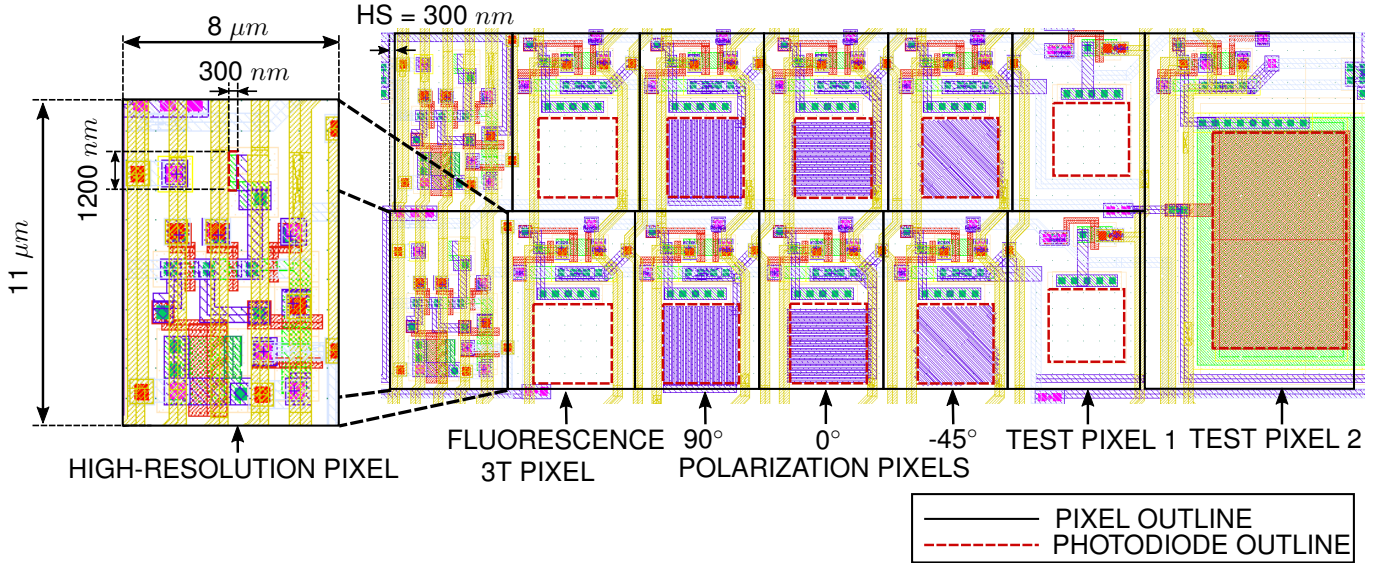


Fig. 5: Layout of one spatial period of multimodal pixels (simplified, no light guards included). HS refers to the horizontal shift between two consecutive $11\ \mu\text{m}$ -height rows of pixels.

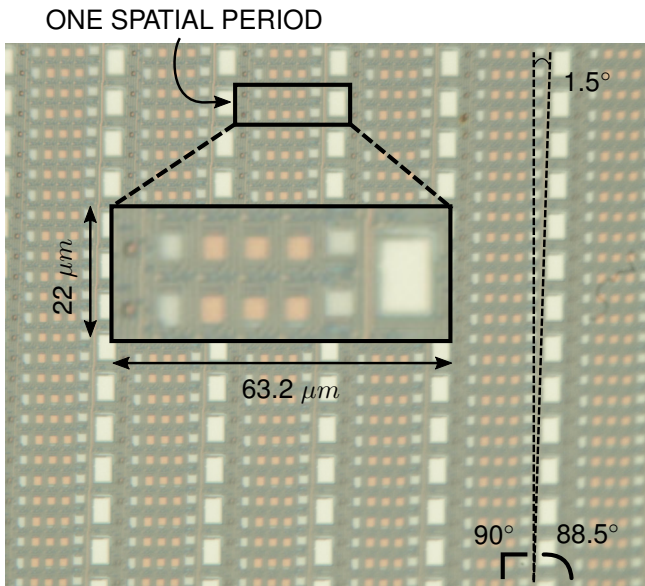


Fig. 6: Micrograph of a segment of the fabricated staggered pixel array prototype. The inset corresponds to the layout in Fig. 5.

256 output columns. The columns are multiplexed to 128 $\Delta\Sigma$ -modulated ADCs. 128 on-chip decimation filters drive 14-bit digital outputs which pass through the 128:1 output multiplexer to off-chip circuitry.

A. Multimodal Pixels

As discussed in Section I, most conventional bench-top microscopes are bulky and expensive, and their optics are typically suited for only one particular type of imaging at a time. For example, a bright-field microscope cannot be used

TABLE II: Summary of the implemented pixel types. Each unit pixel corresponds to a pixel occupying a unit $8\ \mu\text{m} \times 11\ \mu\text{m}$ area except for *Test pixel 2*.

	Pixel Type/Application	Pixel Size (μm^2)	Photodiode Dimensions (μm^2)
1	High-resolution	8×11	0.3×1.2
2	Fluorescence 3t	8×11	5×5
3	90° Polarization	8×11	5×5
4	0° Polarization	8×11	5×5
5	-45° Polarization	8×11	5×5
6	Test pixel 1	8×11	4.7×4.7
7	Test pixel 2	15.2×22	8.7×13.5

to also simultaneously sense the changes in light polarity of a sample. The folded-staggered multimodal image sensor array is used to include five different pixel types, each suitable for a specific imaging modality, while providing a resolution comparable to or slightly worse than that of a conventional microscope. Fig. 5 shows a simplified layout of one period of all pixel types. Table II gives a brief summary of the pixel types. Fig. 6 shows a microscopic image of part of the staggered array.

The size of the photodiode aperture opening is chosen based on several considerations. Without a conventional lens a photodiode aperture opening acts as a pinhole. If the opening is too large, its geometry causes reduced imaging resolution. If

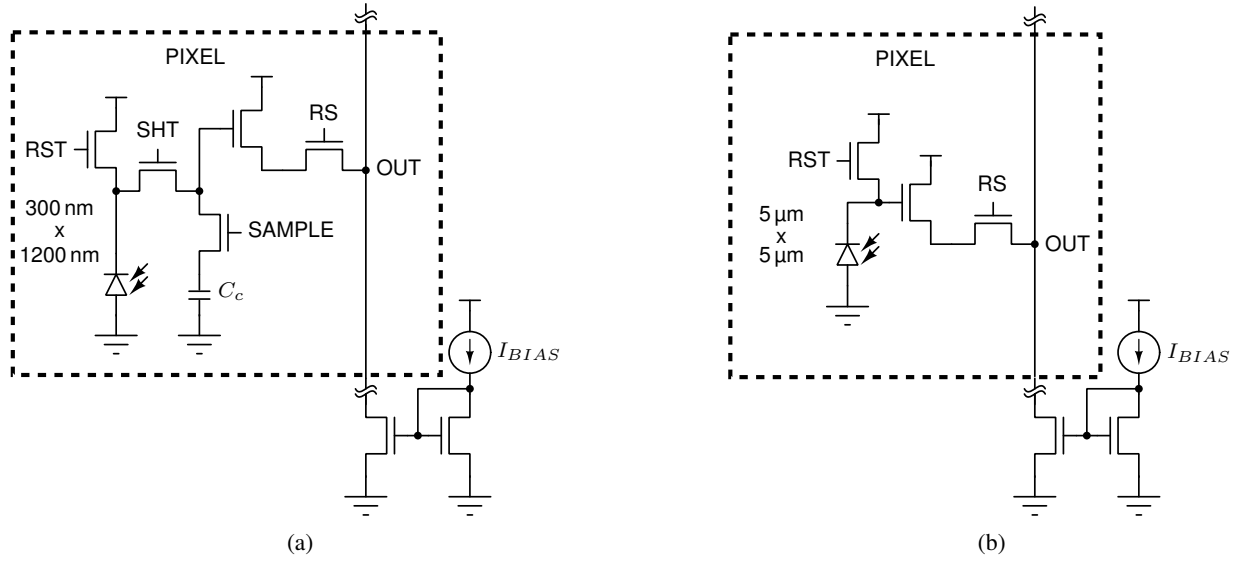


Fig. 7: a) Circuit diagram of the high-resolution small-aperture pixel. b) Circuit diagram of the 3T fluorescence and polarization sensing pixels.

the opening is too small, diffraction effects cause reduced resolution. The minimum size of a pinhole is limited by the light diffraction limit at a given wavelength, and is equal to half of the wavelength: 200 nm to 350 nm for the visible light range of 400 nm to 700 nm. The optimum size of the photodiode opening is given by Rayleighs equation: $d = 1.9 \times \sqrt{f \times \lambda}$, where d is the size of the hole, f is the focal length (the distance from the aperture opening to the photodiode), and λ is the wavelength of light. Assuming the thickness of a metal layers stack of 1-10 microns in various CMOS technologies, for the visible wavelengths range of 400 nm to 700 nm, this leads to the range of optimum pinhole sizes of approximately 1-5 microns. Based on these considerations the following sizes were chosen: the photodiode opening of the left-most pixel in Fig. 5 is chosen to be a 300 nm \times 1200 nm rectangle for near-diffraction-limit imaging in the horizontal dimension and near-optimum sizing in the vertical dimension. The geometry of the rest of the photodiode apertures (with the exception of test pixel 2) is chosen to be a near-optimum 5-micron square.

The imaging modalities which are included in this system are as follows:

1) *High-resolution bright-field imaging*: In bright-field imaging, a high-power light source is assumed for illuminating the sample. Therefore, the specialized pixel for this modality can be optimized for resolution, while sacrificing sensitivity. The circuit diagram is shown in Fig. 7a. As discussed above, the photodiode is a compact n+/p-sub diode, sized only 300 nm \times 1200 nm. It is designed to be small and narrow to minimize the pixel's light sensitive region size to maximize resolution in the horizontal direction. A transfer gate switch is included to enable global shutter or true correlated double sampling (true-CDS) operations. An extra capacitor is used as well to enable two different gain modes for this type of pixel.

2) *3T Fluorescence-sensing pixel*: This is mostly a conventional 3T active pixel. An N-well/p-sub photodiode is used because of its better sensitivity compared to other structures

in standard CMOS technologies [22]. The circuit topology for this pixel is shown in Fig. 7b. The RST signal resets the photodiode and its capacitance to VDD. The light integration is started as soon as RST signal is released. At the end of the integration period, the output of the photodiode is read through a source-follower and a switch controlled by SEL.

Fluorescence sensing is commonly performed by on-CMOS filter deposition. We have previously realized this at the die level using a 40+ dielectric layer interference filter [23], but as a single sheet covering all pixels. Today, pixel-wise emission filter deposition is routinely performed at the wafer scale using lithography in commercially-available products [24]. At the wafer scale, a long-pass multi-dielectric emission filter is typically utilized. According to [24], a filter is deposited on top of the CMOS wafer utilizing a patterned lift-off process. The high-index and low-index dielectric materials are TiO_2 and SiO_2 , respectively, with the top surface being SiO_2 . The filter coating is index matched to water at the peak of emission. As we did not have access to wafers (only 20 dies were available) we did not pursue a pixel-wise fluorescent filter deposition.

3) *Polarization imaging*: Observing the polarity of the light emitted from a specimen provides a richer description of its structure. In this work, three pixel types were allocated to implement on-chip polarization filters to measure the polarity of input light along the three orientations. Each polarization filter is composed of periodic gratings with a width and pitch comparable to the wavelength of the input light illuminated onto the photosensor.

To maximize the polarization properties of the grating, $\frac{\Lambda}{\lambda}$ must be minimized, where λ is the wavelength of the input light and Λ is the grating period [25]. In this work, a grating period of approximately 0.15λ to 0.2λ was implemented. At the risk of design rules checker (DRC) violations, a metal grating with a pitch of 100 nm was implemented using the METAL-1 layer which makes this polarizer suitable for input light in the green ($\lambda = 532$ nm) to red ($\lambda = 620$ nm) region of

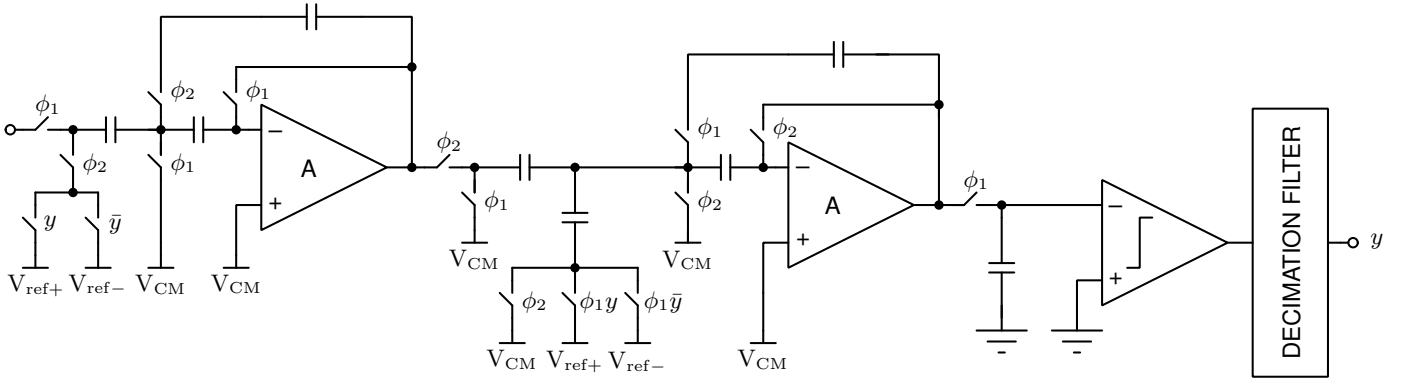


Fig. 8: Second-order $\Delta\Sigma$ modulated ADC circuit.

the visible spectrum. Three pixels identical to the conventional 3T pixel were laid out beside each other. A grating was then added over the photodiode of each pixel. Each grating was rotated to implement one of the three orientations: 90° , 0° and -45° .

B. Readout Circuit

The readout stage is composed of two sections as shown in Fig. 4, namely, the ADC bank and the output multiplexer. The ADCs are column-parallel, organized as 8 banks, with 16 ADCs per bank. Therefore, there are a total of 128 ADCs for 256 pixel columns. For reading out each row, first the odd columns are digitized and sent off-chip, followed by the even columns.

1) *ADC Bank*: A second order $\Delta\Sigma$ ADC is used to accommodate the analog output voltages from the pixel array. The input range of the ADC is from 0.4V to 2.8V, which matches the output range of the pixels. 10-bits of resolution is required based on the noise calculations of [26]. The conversion speed of the ADC is calculated to meet the frame rate requirement, determined by the desired moving speed of the sample.

Second order modulation was chosen for the ADC architecture due to superior speed and idle tone behaviour compared to first order modulation. The modulator consists of two discrete-time integration stages and a one-bit quantizer, as shown in Fig. 8.

Oversampling ratio (OSR) is defined as the ratio with which the input is sampled with respect to the Nyquist rate, and may be written as:

$$OSR = \frac{f_s}{2f_B}$$

where f_s is the sampling frequency and f_B is the bandwidth of the input. An OSR of 125 was chosen to achieve a SNR of 60 dB from an ideal second order $\Delta\Sigma$ modulator with a 1-bit quantizer, while accounting for thermal noise and harmonics in the system. To lower harmonic distortion, and to ensure the loop function's zero shifts due to finite gain are negligible, opamp gain A was set to 70 dB.

2) *Output Multiplexer*: The output multiplexer guides the digitized columns of a particular row to the outputs of the

chip. As mentioned earlier, the ADC bank consists of 8 banks, with 16 ADCs per bank. The output multiplexer consists of two stages: stage-1 multiplexes the ADCs in each bank while stage-2 multiplexes the ADC banks. A desired pixel type can be efficiently selected by setting the *TypeSel* control signal to the desired value. Also, since the pixels are laid out as folded-staggered line sensors, the size of the sample determines what region of the pixel array is used. For a known sample size, power is saved by selecting the appropriate ADC banks which correspond to the chip region over which the sample is moving. This is conveniently set by setting the range of the *BankSel* control signal. If the single desired modality and the sample size are known, readout is performed with no switching in the multiplexer, reducing the total power consumption by approximately 30%.

Given the sampling rate of 1 MHz and the OSR of 125, the effective Nyquist sampling rate is 7.8 ksp/s. Each ADC is shared by two 214-pixel columns, yielding the maximum scan rate of approximately 18 scans per second (55 ms per scan). Accounting for the integration time (conservatively assumed to be 10 ms but depends on lighting conditions and is typically much less to reduce blurring effects at higher flow rates), the nominal scan rate is 15 full scans per second (66 ms). For non-overlapping scans, assuming an object flows near the photodiode aperture plane, this corresponds to the maximum fluid speed of $18 \mu\text{m/s}$ for pixels with 1.2 micron photodiode height and $75 \mu\text{m/s}$ for pixels with 5 micron photodiode height. Such a speed, in fact, not only yields high spatial resolution in the vertical dimension but, being relatively low, also maintains the flow to be laminar (it is already very laminar in micro-scale long fluidic devices). This means an object such as a 15-micron living cell, depending on the photodiode height of the chosen pixel type, can be imaged within 0.2 to 1 seconds. So, at such speeds several conflicting objectives are achieved: reasonably fast scanning, high spatial resolution and laminar flow. Various ways to generate and maintain such flow rates exist, including by reusing some of the photodiodes for motion estimation.

If a higher frame rate and/or further reduced power consumption is required, the row decoder can be configured to read fewer rows, corresponding to a fewer number of sub-pixel

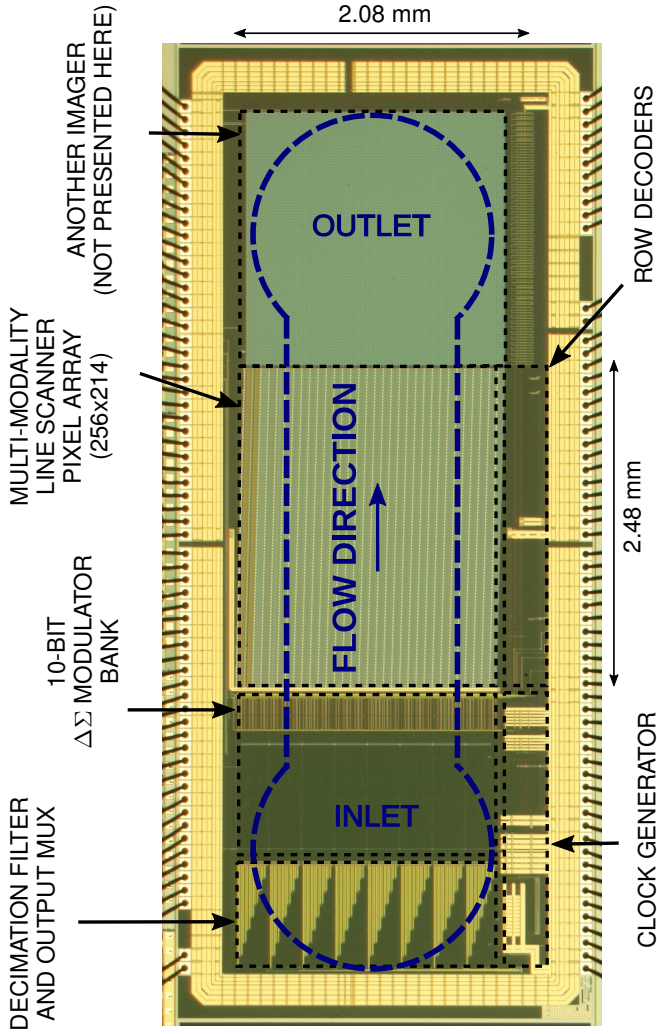


Fig. 9: Micrograph of the $3.2 \text{ mm} \times 7.5 \text{ mm}$ CMOS scanning microscope integrated circuit fabricated in a $0.35 \mu\text{m}$ CMOS image sensor process. An example microfluidic channel position is labelled in blue, as corresponding to the technique depicted in Fig 1, but using one straight channel.

shifted images. For example, if the $3k$ -th rows are excluded from readout in Fig. 3c, this results in two horizontally shifted images instead of three. Of course, this comes at the cost of fewer inputs to the SRA, and in turn, a lower end resolution.

V. MEASUREMENT RESULTS AND DISCUSSION

A micrograph of the CMOS scanning microscope integrated circuit prototype is depicted in Fig. 9. The image sensor was fabricated in a $0.35 \mu\text{m}$ CMOS image sensor process and measures $3.2 \text{ mm} \times 7.5 \text{ mm}$. The input-output pads are located on the left and right sides only. The top and bottom of the die do not include bonding pads to enable easier access for placing a microfluidic chamber or for contact-sliding a dry sample being scanned. To illustrate the microfluidic scanning concept, an example of a microfluidic channel position is labelled in blue in Fig. 9. This corresponds to the techniques depicted in Fig. 1, but using one straight channel, not a maze. The PDMS inlet and outlet are sealed against the die surface

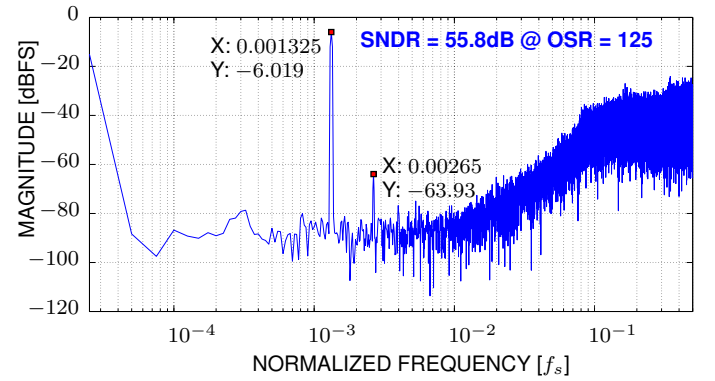


Fig. 10: Experimentally measured output spectrum of the second-order $\Delta\Sigma$ ADC.

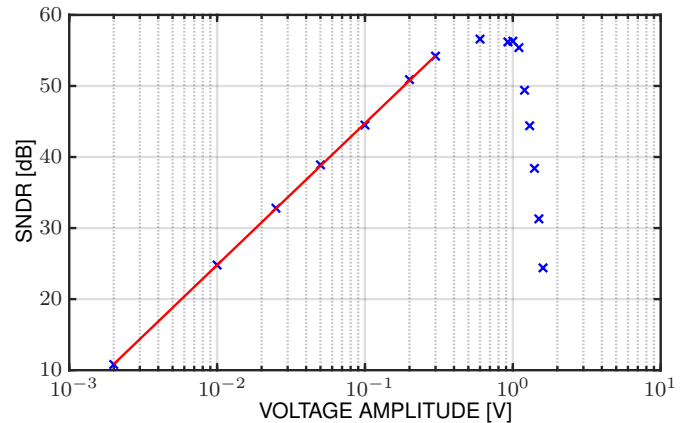


Fig. 11: Experimentally measured SNDR vs input voltage amplitude of the second-order $\Delta\Sigma$ ADC.

over peripheral circuits: the ADC converter, at the bottom, and another imager design, at the top, (not presented here). A sample flows over the $2.08 \text{ mm} \times 2.48 \text{ mm}$ 256×214 -pixel multimodal line scanning array in the middle of the chip, located directly under the fluidic channel.

As detailed in Section II-B, in principle, the direction of the imaged object movement does not need to be perfectly perpendicular to the pixel rows orientation, but would require additional complexity in the image reconstruction algorithm and may reduce the imager resolution. To address these issues, it is important to ensure that the flow in the channel is laminar, so that the motion of any objects in the fluid is orderly with objects in the channel, including close to the channel surfaces, moving in straight lines parallel to that surface. Laminar flow is easier to establish when the aspect ratio (length to width ratio in Fig. 9) of channel geometry is increased. This can be accomplished by narrowing the channel (or introducing multiple narrow channels). Alternatively, a die can be elongated along the vertical dimension, or embedded into a larger-area carrier so that the inlet and outlet are spaced further apart [27]. A high aspect ratio ensures that eddies causing turbulent flow exists only near the inlet/outlet and do not significantly affect the laminar flow through the rest of the channel. Additionally, the flow rate of the fluid should be constant and its value carefully considered as a trade-off

TABLE III: Summary of the ADC specifications and experimentally measured results.

ADC architecture	2nd-order $\Delta\Sigma$
Sampling rate	1 MHz
Bandwidth	4 kHz
Full-scale voltage	0.4 V to 2.8 V
Conversion rate	7.8k samples/sec
Power	60 μ W
PSNR	78 dB
PSNDR	56.6 dB
ENOB	9.1 bits

exists: on the one hand a slower rate of flow makes the flow more laminar, on the other hand, it requires the imaged object properties to be less time-varying (within the scanning time frame; i.e., more solid) and leads to a lower scanning rate.

The output spectrum of the ADC for a voltage input at -6 dBFS is shown in Fig. 10, where the signal to noise and distortion ratio (SNDR) is shown to be limited by the second harmonic. A plot of SNDR versus input amplitude is shown in Fig. 11. The peak SNR of the voltage input is 56.6 dB with a $0.6 V_{pp}$ input. Table III summarizes the specifications of the ADC.

An assembled test printed circuit board (PCB) is depicted in Fig. 12a. In order to emulate a moving sample flowing in a fluidic chamber, a top-to-bottom moving sample image is displayed on a 19-inch Dell UltraSharp 1905FP LCD monitor as shown in Fig. 12b. Both the sensor and monitor were enclosed in a dark chamber. To enable image projection at the micro-scale, a National CCTV 8 mm, $f=1.3$ Micro lens is mounted on the sensor. Sample motion emulation was necessary in order to establish a repeatable-scenario testing platform. Precise sample displacements were obtained by shifting the sample image by a single pixel on the monitor.

The projected sample size was controlled by varying the distance from the monitor to the image sensor. The sizes of the monitor pixels and sensor pixels are known, thus the sensor was placed such that a one-pixel shift in the image displayed on the monitor resulted in a sub-pixel shift in the image captured by the sensor. Optimally, one pixel shift in the monitor-displayed image would correspond to a one-pixel shift in the image captured by the sensor, but this is difficult to achieve in an experimental setup as any misalignment would result in aliasing in the output image. Instead, the distance was experimentally chosen by placing the sensor at the (maximum achievable) distance that yielded the minimum aliasing in the output image.

The experimentally measured results for three samples are presented in Fig. 13. Each row represents results from one of the three experimental samples: bubbles in a microfluidic channel (normally $150 \mu\text{m}$ to $200 \mu\text{m}$ in diameter), a water

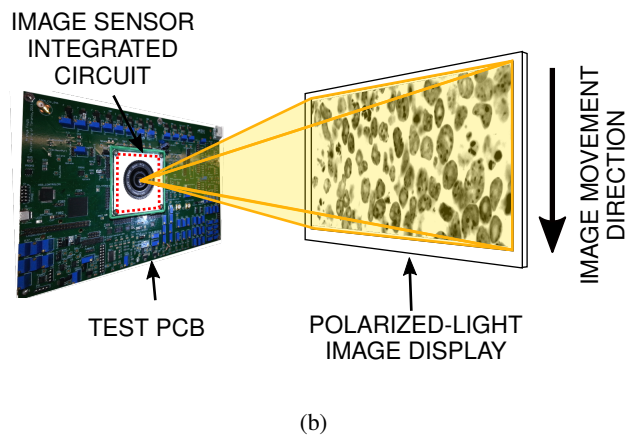
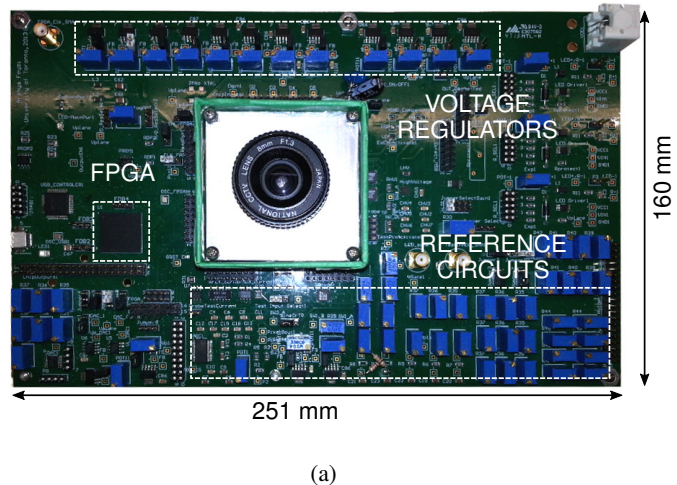


Fig. 12: a) Photograph of the assembled test PCB. b) Diagram of the experimental imaging setup where a sample moving in a fluidic channel is emulated by an image moving on a LCD monitor and projected through a lens.

flea *daphnia pulex* (normally 0.2 mm to 5 mm in length), and mouse embryonic stem cells (normally $5 \mu\text{m}$ to $20 \mu\text{m}$ in size). The originally projected images are in the first column of Fig. 13 - they were projected using the full available monitor projection area. To emulate contact scanning, these samples were displayed on the monitor and shifted pixel-by-pixel downwards as depicted in Fig. 12b. The five subsequent columns represent images reconstructed from the five scanning contact microscope pixel modalities, as follows, left to right from column 2 to column 6: the high-resolution pixel, the fluorescence 3T pixel, and the pixels with 90° , 0° and -45° light polarization filters. The images were reconstructed using the process outlined in Section III. Fixed pattern noise in the images was reduced by applying dark-frame subtraction prior to each image capture session. The vertical line artifacts observable in the reconstructed captured images is a result of inaccuracies and approximations in image reconstruction, and are due in part to discrete steps in the object motion. They can easily be corrected for by spatial low-pass filtering in the horizontal dimension. The brightness and contrast of

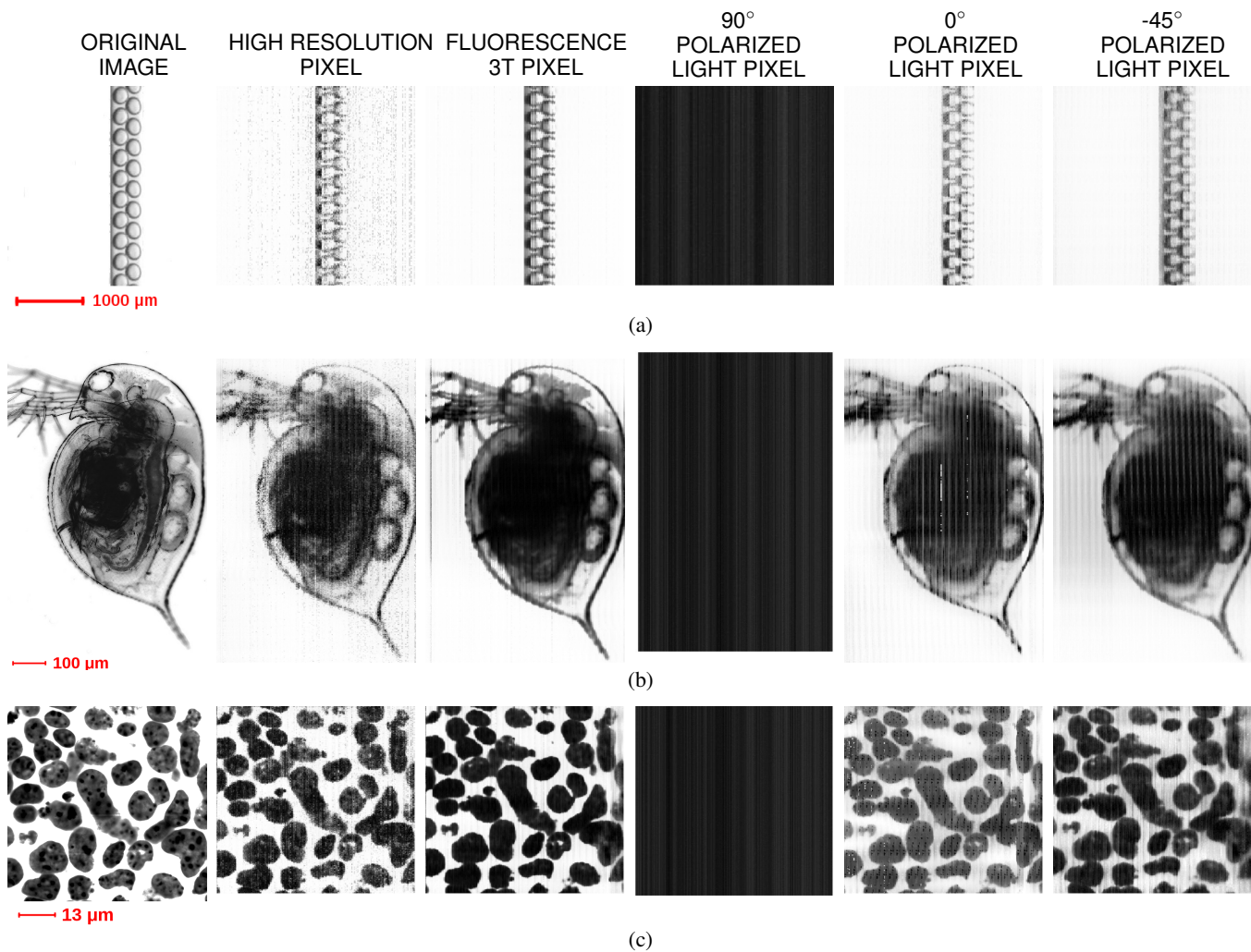


Fig. 13: Experimental results of imaging: a) bubbles in a microfluidic channel, b) *daphnia pulex*, c) mouse embryonic stem cells undergoing osteogenic differentiation. Left to right: column 1 - original image projected from a computer monitor, columns 2-6 images experimentally measured by the presented CMOS multimodal scanning microscope. The scale bars show the approximate sample size, for reference. The actual scanning field-of-view width in all recorded images is 2 mm. The images in columns 2-6 are collected using small photodiodes apertures staggered in the staircase-like fashion as described in Section III and Section IV and are then reorganized to be depicted as conventional 2D images independently of the pixel size (dependent on the photodiode size only), thus validating the sub-pixel resolution imaging capability. Column-to-column FPN was reduced by applying median filtering to column-wise averages of pixel outputs.

the images have been adjusted in post-processing.

The resulting resolution of these images is 300×300 pixels in Fig. 13a, 612×930 pixels in Fig. 13b, and 550×540 pixels in Fig. 13c. These resolution choices are made based on the visual scene spatial spectrum properties and are near the resolution of the LCD monitor (1280×1024 for the entire screen). These images were digitized by the on-chip column-parallel 2nd-order Delta-Sigma ADCs with ENOB of 9.1. They were subsequently reconstructed in software from raw data obtained from the $2.08 \text{ mm} \times 2.48 \text{ mm}$ instantaneous scanning window with a staircase-like staggered-pixels organization. As discussed in Section III, each row of pixels is horizontally shifted by 300 nm to the right with respect to the row below it. This results in the achievable effective spatial resolution in the horizontal dimension of less than the pixel

size, with the theoretical limit of 300 nm. As discussed in Section IV-A1, this is subject to the light diffraction limit and to photodiode size-dependent spatial aliasing (e.g., minimal aliasing for 300 nm-wide photodiodes, with aliasing effect increasing with the photodiode width above 300 nm due to what is effectively a photodiode-to-photodiode overlap in the horizontal dimension). As discussed in Section IV-B2, the spatial resolution in the vertical dimension is set by the sample velocity and the imaging period, as is the case for most scanning sensors, subject to the same limitations.

As no lenses are needed, the cost of such a microscope can be very low (comparable to any integrated circuit fabrication cost, plus the cost of packaging and of the scanning mechanism). This makes the system suitable for both reusable and disposable applications (in cases where chamber contamina-

tion and the corresponding cost of cleaning are a concern).

As expected, the high-resolution pixel (column 2) produces the most spatial details at the expense of a reduced signal, whereas the images from the rest of the pixel types (particularly the fluorescence pixel in column 3) typically have more signal but lower spatial resolution. The last three columns depict the outputs of the light polarization-sensitive pixels. As described in Section IV-A3, a metal grating with a width and spacing of 50 nm each was implemented using the METAL-1 layer for the three orientations: 90°, 0° and -45°. This sizing was (purposefully) in violation of the minimum permitted metal width and pitch by a factor of approximately 10, and as a result the metal gratings were mostly not properly manufactured. For a higher yield, instead of in-CMOS fabricated metal gratings with their known minimum-pitch limitations, fabrication of fine-pitch light polarization filters can be performed after the CMOS fabrication cycle. One such example is using light interference patterns to pattern 70 nm-pitch aluminum nanowires [28]. First a 70 nm thin film of aluminum is deposited, followed by 30 nm thin film deposition of SiO_2 using e-beam evaporation. Two continuous-wave lasers with 266 nm wavelength are aligned to interfere and produce an interference pattern with a period of 140 nm. The interference pattern is transferred to the photoresist. The sample is rotated by 45° each time in order to produce nanowires with four different orientations [28]. In this work, instead of on-chip gratings, off-chip optical polarization filters of 90°, 0° and -45° orientation were used to demonstrate the intended functionality with regards to detection of polarized light. The measured data are depicted in the last three columns in Fig. 13. The monitor emits 0° polarized light, hence the completely dark image obtained with the 90° off-chip filter.

A true-CDS scheme employed in the pixel and the ADC corrects for pixel-to-pixel variations in one column but not for column-to-column fixed pattern noise (FPN). This FPN is particularly prominent in the second column in Fig. 13 where the smallest, 300 nm × 1200 nm, pixel is utilized. Indeed small pixels are harder to match, so higher resolution comes at the cost of higher column-to-column FPN. Given that pixels are staggered, and a pixel can be large even if the photodiode is small, one solution to this issue is a calibration technique such as the one proposed in [29] where additional circuits are included in the pixel. In the presented work, column-to-column FPN was reduced by applying median filtering to the average of the column pixel outputs, as shown in Fig. 13. As discussed, the remaining vertical lines are mostly due to discrete steps in motion of the imaged objects.

VI. CONCLUSION

This paper introduces a concept and VLSI architecture of a low-cost multimodal scanning contact microscope with sub-pixel imaging resolution. As a proof of concept, five imaging sensory modalities are included. Their experimental validation is also presented.

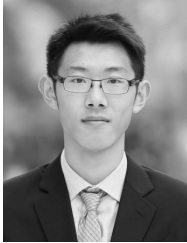
REFERENCES

- [1] M. W. D. Joel S. Silfies, Stanley A. Schwartz, "The diffraction barrier in optical microscopy," tech. rep., Nikon Instruments Inc., 2017.

- [2] K. C. A. Smith and C. W. Oatley, "The scanning electron microscope and its fields of application," *British Journal of Applied Physics*, vol. 6, no. 11, p. 391, 1955.
- [3] B. Smith and T. Zimmerman, "Contact microscope using point source illumination," May 3 2011. US Patent 7,936,501.
- [4] N. T. Shaked, "Visualizing transparent biology with sub-nanometer accuracy," tech. rep., SPIE Newsroom, 2012.
- [5] R. R. Singh, L. Leng, A. Guenther, and R. Genov, "A CMOS-microfluidic chemiluminescence contact imaging microsystem," *Solid-State Circuits, IEEE Journal of*, vol. 47, no. 11, pp. 2822–2833, 2012.
- [6] D. Ho, G. Gulak, and R. Genov, "CMOS 3-T digital pixel sensor with in-pixel shared comparator," in *Circuits and Systems (ISCAS), 2012 IEEE International Symposium on*, pp. 930–933, IEEE, 2012.
- [7] A. Olyaei and R. Genov, "Focal-plane spatially oversampling CMOS image compression sensor," *Circuits and Systems I: Regular Papers, IEEE Transactions on*, vol. 54, no. 1, pp. 26–34, 2007.
- [8] Y. Chae, J. Cheon, S. Lim, M. Kwon, K. Yoo, W. Jung, D.-H. Lee, S. Ham, and G. Han, "A 2.1 M pixels, 120 frame/s CMOS image sensor with column-parallel ADC architecture," *Solid-State Circuits, IEEE Journal of*, vol. 46, no. 1, pp. 236–247, 2011.
- [9] A. Nilchi, J. Aziz, and R. Genov, "Focal-plane algorithmically-multiplying CMOS computational image sensor," *IEEE Journal of Solid-State Circuits*, vol. 44, pp. 1829–1839, June 2009.
- [10] S. Isikman, W. Bishara, H. Zhu, and A. Ozcan, "Optofluidic tomography," in *Frontiers in Optics*, p. FMA4, Optical Society of America, 2011.
- [11] W. Bishara, T.-W. Su, A. F. Coskun, and A. Ozcan, "Lensfree on-chip microscopy over a wide field-of-view using pixel super-resolution," *Optics express*, vol. 18, no. 11, pp. 11181–11191, 2010.
- [12] G. Zheng, S. A. Lee, S. Yang, and C. Yang, "Sub-pixel resolving optofluidic microscope for on-chip cell imaging," *Lab on a Chip*, vol. 10, no. 22, pp. 3125–3129, 2010.
- [13] W. Bishara, S. O. Isikman, and A. Ozcan, "Lensfree optofluidic microscopy and tomography," *Annals of biomedical engineering*, vol. 40, no. 2, pp. 251–262, 2012.
- [14] X. Cui, L. M. Lee, X. Heng, W. Zhong, P. W. Sternberg, D. Psaltis, and C. Yang, "Lensless high-resolution on-chip optofluidic microscopes for caenorhabditis elegans and cell imaging," *Proceedings of the National Academy of Sciences*, vol. 105, no. 31, pp. 10670–10675, 2008.
- [15] H. Zhu, O. Yaglidere, T. Su, D. Tseng, and A. Ozcan, "Cost-effective and compact wide-field fluorescent imaging on a cell-phone," *Lab on a Chip*, vol. 11, pp. 315–22, 11 2010.
- [16] D. N. Breslauer, R. N. Maamari, N. A. Switz, W. A. Lam, and D. A. Fletcher, "Mobile phone based clinical microscopy for global health applications," *PLOS ONE*, vol. 4, pp. 1–7, 07 2009.
- [17] N. A. Switz, M. V. D'Ambrosio, and D. A. Fletcher, "Low-cost mobile phone microscopy with a reversed mobile phone camera lens," *PLOS ONE*, vol. 9, pp. 1–7, 05 2014.
- [18] A. Van Arendonk and C. Draijer, "Wide format sensor," May 10 2012. US Patent App. 13/373,120.
- [19] O. Nixon, "Dual line integrating line scan sensor," Aug. 3 2004. US Patent 6,770,860.
- [20] S. Boyd and D. Qian, "Spatially offset, row interpolated image sensor," Dec. 26 2000. US Patent 6,166,831.
- [21] J. Allen, "Color sensing CCD with staggered photosites," Feb. 19 1991. US Patent 4,994,907.
- [22] K. Murari, R. Etienne-Cummings, N. Thakor, and G. Cauwenberghs, "Which photodiode to use: A comparison of CMOS-compatible structures," *Sensors Journal*, vol. 9, no. 7, pp. 752–760, 2009.
- [23] R. R. Singh, D. Ho, A. Nilchi, G. Gulak, P. Yau, and R. Genov, "A CMOS/thin-film fluorescence contact imaging microsystem for DNA analysis," *IEEE Transactions on Circuits and Systems I: Regular Papers*, vol. 57, pp. 1029–1038, May 2010.
- [24] A. Manickam, R. Singh, M. W. McDermott, N. Wood, S. Bolouki, P. Naraghi-Arani, K. A. Johnson, R. G. Kuimelis, G. Schoolnik, and A. Hassibi, "A fully integrated CMOS fluorescence biochip for DNA and RNA testing," *IEEE Journal of Solid-State Circuits*, vol. 52, pp. 2857–2870, Nov. 2017.
- [25] X. Wu, M. Zhang, N. Engheta, and J. Van der Spiegel, "Design of a monolithic CMOS image sensor integrated focal plane wire-grid polarizer filter mosaic," in *Custom Integrated Circuits Conference (CICC), 2012 IEEE*, pp. 1–4, IEEE, 2012.
- [26] A. Olyaei, "Vipro: Focal-plane CMOS spatially-oversampling computational image sensor," Master's thesis, University of Toronto, 2006.
- [27] Y. Huang and A. J. Mason, "Lab-on-cmos: Integrating microfluidics and electrochemical sensor on cmos," in *2011 6th IEEE International*

Conference on Nano/Micro Engineered and Molecular Systems, pp. 690–693, Feb 2011.

- [28] V. Gruev, R. Perkins, and T. York, “CCD polarization imaging sensor with aluminum nanowire optical filters,” *Optics Express*, vol. 18, pp. 19087–19094, 8 2010.
- [29] J. Yuan, H. Y. Chan, S. W. Fung, and B. Liu, “An activity-triggered 95.3 db dr –75.6 db thd cmos imaging sensor with digital calibration,” *IEEE Journal of Solid-State Circuits*, vol. 44, pp. 2834–2843, Oct 2009.



Chengzhi Winston Liu received the B.A.Sc. degree in Engineering Science, majoring in Robotics Engineering, from the University of Toronto in 2018. From 2016 to 2017, he was a Software/Hardware Intern at Zebra Technologies, Mississauga, Canada. Previously, from 2011 to 2014, he completed multiple internships at Evertz Microsystems in Burlington, Canada, where he was involved in the FPGA design of video broadcasting products.



Arshya Feizi (S’10) received his B.Sc degree in Electrical and Computer Engineering from the University of Tabriz, Tabriz, Iran in 2011 and his M.A.Sc in Electrical and Computer Engineering from University of Toronto, Toronto, Canada in 2014. His research interests include CMOS image sensors for biomedical imaging and oversampling ADCs.

Arshya worked for Analog Devices Inc. from 2014 to 2017 as a mixed-signal design engineer in Boston, Massachusetts. Currently, he is a PhD

student in Operations and Technology Management in Boston University, MA.



Navid Sarhangnejad (S’15) received the B.Sc. degree in Electrical and Computer Engineering from the University of Tehran, Tehran, Iran, in 2008 and the M.S. degree in Electrical and Computer Engineering from Delft University of Technology, Delft, the Netherlands, in 2010.

From 2011 to 2014, he was a Mixed-Signal Design Engineer at CMOSIS, Antwerp, Belgium. He is currently pursuing the Ph.D. degree in Electrical and Computer Engineering at the University of Toronto, Canada. His research interests include analog/mixed-

signal circuits, over-sampled ADCs, and CMOS image sensors.



Glenn Gulak is a Professor in the Department of Electrical and Computer Engineering at the University of Toronto. His research interests are in the areas of algorithms, circuits, and CMOS implementations of high-performance baseband digital communication systems and hardware accelerators. He has authored or co-authored more than 150 publications in refereed journals and conference proceedings, and has received numerous teaching awards at the University of Toronto.



Roman Genov (S’96-M’02-SM’11) received the B.S. degree in Electrical Engineering from Rochester Institute of Technology, NY in 1996 and the M.S.E. and Ph.D. degrees in Electrical and Computer Engineering from Johns Hopkins University, Baltimore, MD in 1998 and 2003 respectively.

He is currently a Professor in the Department of Electrical and Computer Engineering at the University of Toronto, Canada, where he is a member of Electronics Group and Biomedical Engineering Group and the Director of Intelligent Sensory Microsystems Laboratory. Dr. Genov’s research interests are primarily in analog integrated circuits and systems for energy-constrained biological, medical, and consumer sensory applications.

Dr. Genov is a co-recipient of Jack Kilby Award for Outstanding Student Paper at IEEE International Solid-State Circuits Conference, NSERC Discovery Accelerator Award, Best Paper Award by IEEE Transactions on Biomedical Circuits and Systems, Best Paper Award at IEEE Biomedical Circuits and Systems Conference, Best Paper Award in Biomedical Systems and Best Student Paper Award at IEEE International Symposium on Circuits and Systems, Brian L. Barge Award for Excellence in Microsystems Integration, MEMSCAP Microsystems Design Award, DALSA Corporation Award for Excellence in Microsystems Innovation, and Canadian Institutes of Health Research Next Generation Award. He was a Technical Program Co-chair at IEEE Biomedical Circuits and Systems Conference. He was an Associate Editor of IEEE TRANSACTIONS ON CIRCUITS AND SYSTEMS-II: EXPRESS BRIEFS and IEEE SIGNAL PROCESSING LETTERS, and a member of IEEE International Solid-State Circuits Conference International Program Committee. Currently he is an Associate Editor of IEEE TRANSACTIONS ON BIOMEDICAL CIRCUITS AND SYSTEMS, and its Guest Editor of Special Issues on IEEE International Solid-State Circuits Conference.